

Turbulent Clustering of Point Particles and Finite-Size Particles in Isotropic Turbulent Flows

Guodong Jin, Yun Wang, Jian Zhang, and Guowei He*

LNM, Institute of Mechanics, Chinese Academy of Sciences, Beijing 100190, P. R. China

ABSTRACT: Particle clustering in turbulent flows is ubiquitous in particle-fluid two-phase flows in the riser of fast fluidized beds. Controlling the level of clustering is very crucial for improving the reactive efficiency in such flows. The present paper is devoted to numerically studying particle clustering in turbulent flows, where both point particles and finite-size particles are taken into account, respectively. A pseudospectral method with the particle tracking method is used to simulate the point particle clustering in the forced isotropic turbulent flows, while the lattice Boltzmann method is used to simulate the finite-size particles in decaying isotropic turbulent flows. It is observed that the mean drift velocity, caused by forces such as gravity, could reduce the level of particle clustering for point particles. However, the particle clustering is very weak for the particles of sizes larger than the characteristic viscous scales of turbulent flows, which is consistent with the previous experimental results. The observations suggest that the mean drift velocity and particle sizes can be used to control the level of particle clustering in chemical reactors.

1. INTRODUCTION

In the riser of fast fluidized beds used in chemical engineering, heterogeneous flow structures are developing in the particle-fluid two-phase flows due to the competition between particle gravity and fluid drag force according to the energy minimization multiscale (EMMS) theory.¹ Even in a fluid-dominating regime, the heterogeneity at mesoscale exists due to particle interaction with turbulent flows. In the fluid-dominating regime, turbulence plays an important role in the formation of particle clusters. Particle clustering is due to the competition between the inertia of a particle and the centrifugal force acting on particles, where particles tend to accumulate in the regions of high strain rate and low vorticity in turbulent flows. When particle response time τ_p is comparable to the turbulent Kolmogorov time scale τ_K , that is, the particle Stokes number $St_K = \tau_p/\tau_K$ is about 1.0, the particle cluster is most favorable.² Under gravity, particles have a mean relative velocity to the surrounding flows. The relative velocity reduces the interaction time scale between the turbulent structures and particles, thus it could suppress the level of particle clustering in turbulence.^{3,4}

The formation of clusters not only affects the hydrodynamic coupling between the dispersed particles and fluid, but also affects the mass and heat transfer rates between particles and fluid, and thus affects the chemical rate in the fluidized beds.^{5–7} The collision rate between particles can be increased by one order due to the formation of cluster.⁸ Therefore, it is meaningful to control the level of particle clusters using an external body force, such as gravity or electrical forces for charged particles.

The formation of clusters in large-scale reactors raises a challenge to computational fluid dynamics (CFD) simulation. In industrial-scale reactors, the spatial resolution can not be fine enough to fully resolve the mesoscale clusters; the subgrid cluster structures have substantial influences on drag force. In the EMMS framework, many corrections to the drag force formula due to subgrid cluster structures are proposed to

improve the ability of the Eulerian–Eulerian two-fluid models to simulate industrial scale reactors.^{9–12}

Several methods have been used to quantify the clusters formed in turbulent flows, such as the box counting method,¹³ correlation dimension,^{14,15} radial distribution function (RDF) or particle-pair correlation,^{16–18} the Voronoi diagram analysis,^{19–22} and Minkowski functional.²³ The last two methods widely used in cosmology have been recently applied to geometrically characterize clusters of particles in turbulence. Tagawa et al.²¹ first analyzed the Lagrangian autocorrelation of the Voronoi volumes and found that the clustering of light particles lasts much longer than that of heavy or neutrally buoyant particles. Light and heavy particles remain clustered for much longer times than the flow structures which cause the clustering due to the inertial bias between the particle and fluid. Using Minkowski functionals as morphological order parameters, Calzavarini et al.²³ quantified the geometrical and topological features of particle and bubble clusters in turbulent flow. The RDF has the advantage of providing scale by scale quantification of clusters and allowing theoretical calculation of particle collision rate, thus we use the RDF to characterize particle clusters in this paper. We also propose to use wavenumber spectrum of particle concentration fluctuations to analyze the multiscale nature of particle clusters.

The objectives of this paper are to study the Stokes number-dependent clusters of point particles and finite-size particles suspended in turbulent flows and to investigate the effects of a mean relative velocity on particle clustering in isotropic turbulent flows. Two direct numerical simulation (DNS) methods are used to simulate fluid flows: One is based on

Special Issue: Multiscale Structures and Systems in Process Engineering

Received: December 17, 2012

Revised: January 24, 2013

Accepted: January 25, 2013

Published: January 25, 2013

the point particle DNS (PPDNS) for particle diameters much smaller than the turbulent Kolmogorov length scale, in which the Navier–Stokes equations are solved using the pseudospectrum method with artificial forcing at the large scales, and particle motions under a drag force and gravity are tracked using the Lagrangian method. One-way coupling from fluid to particles is assumed. Another method is based on the particle-resolved DNS (PRDNS) for finite-size particles with diameters comparable to or larger than the turbulent Kolmogorov length scale, in which the turbulent flow is solved using the lattice Boltzmann method since this method can easily handle the complex moving boundaries between particles and fluid with a high parallel efficiency.^{24–26} The two-way coupling between particles and fluid are achieved through the momentum exchange at the moving surfaces of particles.

The organization of this paper is as follows. The mathematical models for PPDNS and PRDNS are given in section 2. Numerical results are presented and discussed in section 3. Conclusions are drawn in section 4.

2. MATHEMATIC MODELING

In this section, we first give the method for the point particle DNS (PPDNS), and then, we describe the method for the particle-resolved DNS (PRDNS).

2.1. Point Particle Direct Numerical Simulations.

Currently, a reliable approach for studying the particle-turbulence interactions is the Eulerian–Lagrangian simulations based on the point particle model. In this model, the particle diameters are assumed to be much smaller than the Kolmogorov length scale of turbulent flow and particle motions are described by a model equation which includes the drag force, added mass, and body forces, etc.

2.1.1. Pseudo-Spectrum Method for the Turbulent Flows.

The fluid velocity is governed by the incompressible Navier–Stokes equations

$$\nabla \cdot \mathbf{u} = 0 \quad (1)$$

$$\frac{\partial \mathbf{u}}{\partial t} = \mathbf{u} \times \boldsymbol{\omega} - \nabla \left(\frac{p}{\rho} + \frac{1}{2} u^2 \right) + \nu \nabla^2 \mathbf{u} + \mathbf{f}(\mathbf{x}, t) \quad (2)$$

where \mathbf{u} denotes the fluid velocity, $\boldsymbol{\omega} = \nabla \times \mathbf{u}$ fluid vorticity, p is pressure, ρ is fluid density, and ν is fluid kinematical viscosity. The flow is driven and maintained by a random forcing $\mathbf{f}(\mathbf{x}, t)$ which is nonzero only at low wavenumbers in Fourier space $\|\mathbf{k}\| < \sqrt{8}$.²⁷ In Fourier space, the Navier–Stokes equations can be described as

$$\left(\frac{\partial}{\partial t} + \nu k^2 \right) \hat{\mathbf{u}}(\mathbf{k}, t) = \mathbf{P}(\mathbf{k}) F(\mathbf{u} \times \boldsymbol{\omega}) + \hat{\mathbf{f}}(\mathbf{k}, t) \quad (3)$$

where $\hat{\mathbf{u}}(\mathbf{k}, t)$ is a Fourier coefficient of fluid velocity \mathbf{u} , $\mathbf{k} = (k_1, k_2, k_3)$ is the wavenumber vector. The projection tensor $\mathbf{P}(\mathbf{k})$ projects $\mathbf{u} \times \boldsymbol{\omega}$ onto the plane normal to \mathbf{k} and eliminates the pressure term in eq 2. The term $\mathbf{u} \times \boldsymbol{\omega}$ is calculated using the pseudospectral method. F denotes the Fourier transform.

The flow domain is discretized uniformly into N^3 grid points in a cubic box with each side of 2π ($N = 256$ in this paper). The spatial resolution is monitored by the value of ηk_{\max} , where η is the Kolmogorov length scale, k_{\max} is the maximum cutoff wavenumber, and $k_{\max} = N/3$. This quantity should be larger than unity if the Kolmogorov scale of the flow is well-resolved. The value of ηk_{\max} is typically larger than 1.1 in our simulation. The Fourier coefficients are advanced in time using a second-

order Adams–Bashforth method for the nonlinear term and an exact integration for the linear viscous term. The time step is chosen to ensure that the Courant–Friedrichs–Lewy (CFL) number is 0.5 or less for numerical stability and accuracy.²⁸

2.1.2. Motions of Point Particles. The discrete phase is composed of solid, spherical particles with $d_p < \eta$ and $\rho_f \ll \rho_p$ where ρ_p is particle density. Many forces act on a single particle suspended in turbulent flow fields.²⁹ Since $\rho_f \ll \rho_p$, the forces on a small particle can be simplified as drag force and gravity force. Then, the governing equations for a single particle can be written as

$$\frac{d\mathbf{Y}_p(t)}{dt} = \mathbf{V}_p(t) \quad (4)$$

$$\frac{d\mathbf{V}_p(t)}{dt} = \frac{(\mathbf{u}(\mathbf{Y}_p(t), t) - \mathbf{V}_p(t))f + \mathbf{w}_0}{\tau_p} \quad (5)$$

where \mathbf{Y}_p and $\mathbf{V}_p(t)$ are particle position and velocity at time t , \mathbf{w}_0 is the particle Stokes terminal or settling velocity in still fluid under gravitational acceleration \mathbf{g} , τ_p is particle relaxation time, $\tau_p = d_p^2 \rho_p / 18 \rho_f \nu$, $\mathbf{w}_0 = \tau_p \mathbf{g}$, and d_p is particle diameter. The term $\mathbf{u}(\mathbf{Y}_p(t), t)$ is the fluid velocity seen by a particle. The velocity is obtained from DNS flow field by a three-dimensional six-point Lagrangian interpolation scheme, f is the nonlinear drag correction coefficient,

$$f(Re_p) = 1 + 0.15 Re_p^{0.687} \quad (6)$$

which is determined by the instantaneous value of the particle Reynolds number, $Re_p = |\mathbf{u} - \mathbf{V}_p| d_p / \nu$.

The motion of a particle is obtained by numerical integration using a fourth-order Adams–Bashforth method for the particle velocity and a fourth-order Adams–Moulton method for particle trajectory, respectively.

2.2. Particle-Resolved Direct Numerical Simulation.

When the particle diameter d_p is comparable to or larger than the Kolmogorov length, the point particle model becomes invalid because the particle-fluid slip velocity which governs the motion of a point particle can no longer be properly defined and the equation of particle motion is not available.^{30–32} The limitations of the point particle approach have motivated the development of particle-resolved simulation methods in recent years such as the immersed boundary method (IBM),³³ distributed Lagrange-multiplier (DLM) method,³⁴ and the lattice Boltzmann method.³⁵

2.2.1. Lattice Boltzmann Method. In this paper, the multiple-relaxation-time lattice-Boltzmann equation (MRT-LBE) is used to simulate the isotropic turbulent flows with moving finite-size particles.³⁶ At each lattice point \mathbf{x} and time t , the mesoscale distribution function $\mathbf{f}(\mathbf{x}, t)$ is governed by

$$\mathbf{f}(\mathbf{x} + \mathbf{e}_i \delta_t, t + \delta_t) = \mathbf{f}(\mathbf{x}, t) - \mathbf{M}^{-1} \cdot \mathbf{S} \cdot [\mathbf{m} - \mathbf{m}^{(eq)}] \quad (7)$$

where $\mathbf{f}(\mathbf{x}, t)$ is a vector indicating the distributions of 19 lattice particles in the D3Q19 model, \mathbf{M} is a 19×19 orthogonal transformation matrix which converts the distribution function $\mathbf{f}(\mathbf{x}, t)$ from the discrete velocity space into the moment space \mathbf{m} , where the collision relaxation is performed. The term $\mathbf{m}^{(eq)}$ is the equilibrium value of the moment \mathbf{m} , and δ_t is the time step. The transformations between the particle velocity space and the moment space are

$$\mathbf{m} = \mathbf{M} \cdot \mathbf{f}, \quad \mathbf{f} = \mathbf{M}^{-1} \cdot \mathbf{m}, \quad \mathbf{m}^{(eq)} = \mathbf{M} \cdot \mathbf{f}^{(eq)} \quad (8)$$

The macroscale variables are obtained from the moments of the distribution function

$$\begin{aligned}\rho_{f0} &= 1, & \delta\rho_f &= \sum_i f_i, & \rho_{f0} \mathbf{u} &= \sum_i f_i \mathbf{e}_i, \\ \rho_f &= \rho_{f0} + \delta\rho_f, & p &= \delta\rho_f c_s^2\end{aligned}\quad (9)$$

where \mathbf{u} is the macroscale fluid velocity, ρ_{f0} is the mean density, $\delta\rho_f$ is the density fluctuation, and the discrete velocities \mathbf{e}_i in the D3Q19 model shown in Figure 1 can be expressed as³⁷

$$\mathbf{e}_i = \begin{cases} (0, 0, 0) & i = 0 \\ (\pm 1, 0, 0), (0, \pm 1, 0), (0, 0, \pm 1) & i = 1, 2, \dots, 6 \\ (\pm 1, \pm 1, 0), (\pm 1, 0, \pm 1), (0, \pm 1, \pm 1) & i = 7, 8, \dots, 18 \end{cases} \quad (10)$$

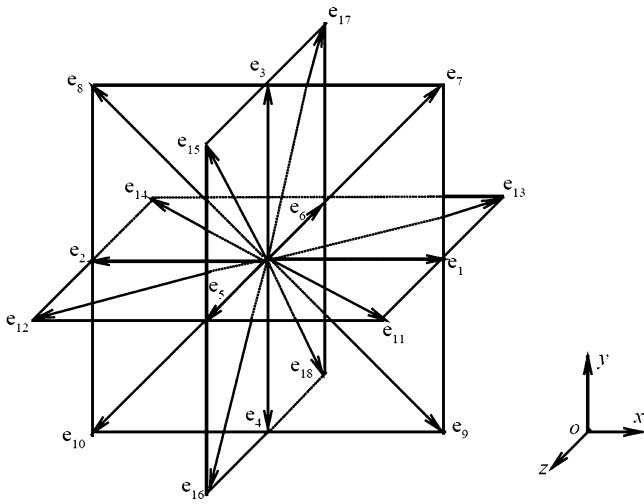


Figure 1. Schematic diagram showing the velocities of 19 lattice particles in the D3Q19 model.

The following equilibrium distribution function is used to initialize the distribution function

$$f_i^{(eq)} = W_i \left(\delta\rho_f + \rho_{f0} \frac{\mathbf{e}_i \cdot \mathbf{u}}{c_s^2} + \rho_{f0} \frac{(\mathbf{e}_i \cdot \mathbf{u})^2}{2c_s^4} - \rho_{f0} \frac{u^2}{2c_s^2} \right) \quad (11)$$

2.2.2. Motions of Finite-Size Particles. Particle motion is governed by the gravity force and the hydrodynamic force of the fluid. An advantage of LBM is that the hydrodynamic force acting on the solid particle is directly calculated based on the impulses exerted on the lattice fluid particles and Newton's third law. The hydrodynamic force \mathbf{F}_{hy} acting on the solid particle is the summation of the loss of the fluid momentum, from t to $t + \delta_t$, on all the links cutting the solid particle surface. The torque $\mathbf{\Gamma}_{hy}$ is the summation of the cross product of the local position vector relative to the center of the particle and the loss of fluid momentum over all boundary links. Namely,

$$\begin{aligned}\mathbf{F}_{hy}^{t+0.5\delta_t} &= \sum_{bn} [\hat{f}_i(\mathbf{x}, t) \mathbf{e}_i - f_{\bar{i}}(\mathbf{x}, t + \delta_t) \mathbf{e}_{\bar{i}}] \\ &= \sum_{bn} [\hat{f}_i(\mathbf{x}, t) + f_{\bar{i}}(\mathbf{x}, t + \delta_t)] \mathbf{e}_i\end{aligned} \quad (12)$$

$$\mathbf{\Gamma}_{hy}^{t+0.5\delta_t} \delta_t = \sum_{bn} \hat{\mathbf{n}}_i \times [\hat{f}_i(\mathbf{x}, t) + f_{\bar{i}}(\mathbf{x}, t + \delta_t)] \mathbf{e}_i \quad (13)$$

where "bn" denotes summation over all boundary links, $\mathbf{e}_{\bar{i}} = -\mathbf{e}_i$, and $\hat{f}_i(\mathbf{x}, t) = f(\mathbf{x}, t) - \mathbf{M}^{-1} \cdot \mathbf{S} \cdot [\mathbf{m} - \mathbf{m}^{(eq)}]$ denotes the distribution function just after the collision (referred to the time step $t + 0.5\delta_t$). $f_{\bar{i}}(\mathbf{x}, t + \delta_t)$ denotes the distribution function after bounce-back collision with the solid particle surface at \mathbf{x} and $t + \delta_t$. $\hat{\mathbf{n}}_i$ denotes the local outward-normal vector connecting the solid particle center and the point of intersection of the i link with the surface of the solid particle. After obtaining the hydrodynamic force and torque acting to a particle, we update the particle transversal velocity $\mathbf{V}_p^{t+\delta_t}$, particle rotational velocity $\Omega_p^{t+\delta_t}$, particle transversal displacement $\mathbf{Y}_p^{t+\delta_t}$, and particle angular displacement $\Theta_p^{t+\delta_t}$, respectively, by

$$\begin{aligned}\mathbf{V}_p^{t+\delta_t} &= \mathbf{V}_p^t + \frac{1}{2M_p} [(\mathbf{F}_{hy} + \mathbf{F}_{lub}^{t+\delta_t/2} \\ &\quad + (\mathbf{F}_{hy} + \mathbf{F}_{lub}^{t-\delta_t/2}) \delta_t + (\rho_p - \rho_f) \mathbf{g} \delta_t]\end{aligned} \quad (14)$$

$$\Omega_p^{t+\delta_t} = \Omega_p^t + \frac{1}{2I_p} [\mathbf{\Gamma}_{hy}^{t+\delta_t/2} + \mathbf{\Gamma}_{hy}^{t-\delta_t/2}] \delta_t \quad (15)$$

$$\mathbf{Y}_p^{t+\delta_t} = \mathbf{Y}_p^t + 0.5(\mathbf{V}_p^t + \mathbf{V}_p^{t+\delta_t}) \delta_t \quad (16)$$

$$\Theta_p^{t+\delta_t} = \Theta_p^t + 0.5(\Omega_p^t + \Omega_p^{t+\delta_t}) \delta_t \quad (17)$$

where M_p denotes the mass of the particle, I_p is the moment of inertia of the particle, \mathbf{g} is the gravitational acceleration, and \mathbf{F}_{lub}^c represents the lubrication force correction, to be described below.

2.2.3. Particle–Particle Hydrodynamic Interactions in Short Range. When the gap between two particles is less than about 2 lattice units, the local viscous flow in the gap is not adequately resolved, leading to underestimation of hydrodynamic force. Here, we use the stiffness-based elastic model to correct the short-range particle–particle hydrodynamic interactions³⁸

$$\mathbf{F}_{lub}^c = \begin{cases} 0, & r_{ij} > d_p + \varsigma \\ c_{ij} \left(\frac{r_{ij} - d_p - \varsigma}{\varsigma} \right)^2 \left(\frac{\mathbf{r}_{ij}}{r_{ij}} \right), & r_{ij} \leq d_p + \varsigma \end{cases} \quad (18)$$

where $\mathbf{r}_{ij} = \mathbf{Y}_{pi} - \mathbf{Y}_{pj}$, $r_{ij} = |\mathbf{Y}_{pi} - \mathbf{Y}_{pj}|$, c_{ij} is set to be buoyancy force. ϵ_p is an adjustable parameter.

3. NUMERICAL RESULTS AND DISCUSSIONS

3.1. Turbulent Flows. When the flow reaches a statistically stationary flow state, the energy spectrum of the flow displays a short inertial subrange as shown in the spectrum in Figure 2. Table 1 lists the statistics of the isotropic turbulent flows simulated, where N^3 is the space resolution of flow domain of $(2\pi)^3$, $Re_\lambda \equiv u' \lambda / \nu$ is the Reynolds number based on the Taylor microlength scale λ . Here, $\lambda = u' / \langle (\partial u_i / \partial x_i)^2 \rangle^{1/2}$, u' is the root-mean-square (rms) of the velocity, ϵ is the energy dissipation rate per unit mass, L_f is the integral length-scale, $L_f = u'^3 / \epsilon$. Also, $\eta \equiv (\nu^3 / \epsilon)^{1/4}$ and $\tau_K \equiv (\nu / \epsilon)^{1/2}$ are the Kolmogorov length and time scales, respectively, $K_{max} = N/3$ is the cutoff wavenumber in the pseudospectral method.

3.2. Point Particle Clustering. Inertial particles are expelled from regions of high vorticity due to the centrifugal

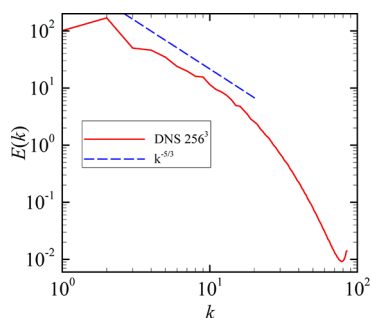


Figure 2. Spectrum in forced isotropic turbulence at Reynolds number $Re_\lambda = 100.9$.

force and preferentially concentrate in regions of low vorticity and high strain rate in turbulent flows. Figure 3 shows the clustering of inertial particles in a 2D snapshot centered at the 3D flow field at $z = \pi$ where particle Stokes number is $St_K = 1.0$. In the figure, the regions of red and blue colors denote the positive and negative high vorticities respectively and the regions of green color denote low vorticity. We can observe that particles mainly distribute in the green regions. We use the radial distribution function at contact $g(R)$ to quantify the clustering which indicates the probability of finding a particle pair separated by a distance $R = d_p$, with respect to the probability of finding a particle pair in a uniformly distributed field. The term $g(R)$ is simply computed as

$$g(R) = \frac{N_{\text{pair}}(R)/V_{\text{shell}}}{0.5N_p(N_p - 1)/(2\pi)^3} \quad (19)$$

where $N_{\text{pair}}(R)$ is the number of particle pairs located in the shell $V_{\text{shell}} = 4\pi[(R + \delta R)^3 - R^3]/3$ with a reference particle at the center, R and $R + \delta R$ as radii, and $\delta R = 0.05R$ in this study.

Figure 4 shows that there are three regimes for $g(R)$. In the limit cases of both $St_K \rightarrow 0$ and $St_K \rightarrow \infty$, particles tend to be uniformly distributed and $g(R) \rightarrow 1$ since particles with a very small Stokes number are distributed like fluid elements and particles with a very large Stokes number are not responsive to flow structures. For the intermediate Stokes numbers, particles interact with a range of fluid eddies and tend to accumulate in the regions of low vorticities shown in Figure 3, leading to the large values of $g(R)$ with a peak value around $St_K = 1$ in the DNS. This trend is consistent with the previous observations.³⁹

From Figure 3, we can also observe that the length-scale of the cluster structure is not uniform and manifests a characteristic of multiscale. In general, the particle concentration field changes with Stokes number and contains more large-scale structures as the Stokes number increases. When the particle relaxation time is comparable to the time scale of a certain length-scale of eddies, clusters mainly form around those eddies, and the characteristic length-scale of the cluster reflects the length-scale of that eddy. Like the energy spectrum of turbulent fluctuating velocity, we can analyze the multiscale nature of the clusters using the energy spectrum of particle concentration fluctuation. This is demonstrated in Figure 5 which plots the energy spectra of concentration fluctuations at

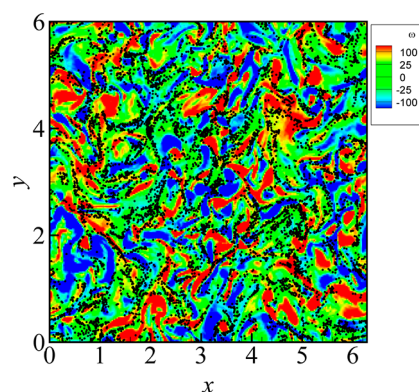


Figure 3. Snapshot of particle clustering in a 3D flow field at $St_K = 1.0$.

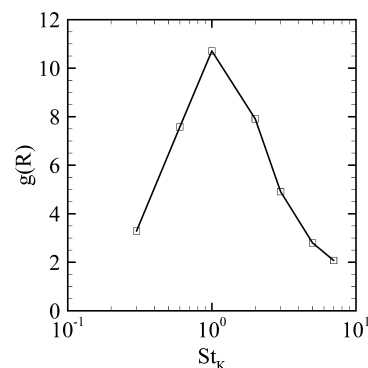


Figure 4. Variation of the level of clustering $g(R)$ with particle Stokes number.

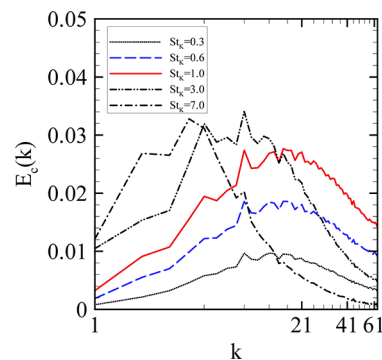


Figure 5. Wavenumber spectra of particle concentration fields.

the Stokes numbers $St_K = 0.3, 0.6, 1.0, 3.0, 7.0$, ranging from small to large inertial particles. The particle concentration $C(\mathbf{x}, t)$ is defined as the number of particles in a local grid centered at \mathbf{x} . In the present calculations, 128^3 coarse grids are used to compute the particle concentration field. The difference between the particle concentration $C(\mathbf{x}, t)$ at time t and the initial concentration $C(\mathbf{x}, 0)$ is defined as the concentration fluctuations. Since the probability distribution function (PDF) of $C(\mathbf{x}, 0)$ is a Poisson distribution, the difference $\Delta C = C(\mathbf{x}, t) - C(\mathbf{x}, 0)$ measures the fluctuations of concentration relative to a randomly uniform concentration. When particle concen-

Table 1. Statistical Parameters in the Isotropic Turbulent Flows

N^3	Re_λ	ε	ν	u'	L_f	λ	v_K	τ_K	$\eta_{k_{\max}}$
256^3	100.9	4834.7	0.049	19.52	1.54	0.24	3.62	0.0037	1.06

tration field becomes statistically stationary, the concentration fluctuations are transformed into the Fourier space. The area under each curve in Figure 5 denotes the concentration variance of heavy particles. It measures the degree of nonuniformity of the particle concentration for a given Stokes number. This area increases with St_K , reaches a maximum at $St_K = 1$, then decreases with St_K . It is observed from Figure 5 that as the Stokes number increases, the peaks of concentration spectra move from larger wavenumbers to smaller ones with more concentration energy contained at small wavenumbers. The peak wavenumber gives an indication of the length scale at which these eddies contribute most significantly to the concentration field.

3.3. Controlling Particle Clustering and Collision.

When particles move in isotropic turbulent flows under gravity, there is a mean drift velocity between the particles and the surrounding turbulent flows. The mean drift velocity will drive the particle away from the regions of low vorticity and reduce the interaction time between particles and turbulence. Thus, particles will distribute more uniformly in the flows fields. This is qualitatively demonstrated in Figure 6 which plots the

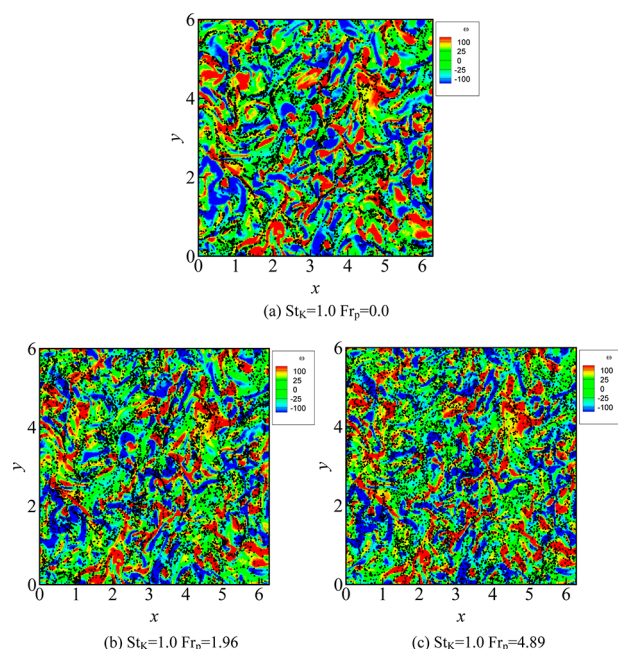


Figure 6. Particle clustering at different Froude numbers.

variation of particle preferential concentration with the Froude number which is defined as $Fr_p = w_0/u'$, the ratio of particle settling velocity to the fluid fluctuation velocity. We can observe the tendency that the level of clustering is reduced with increasing the Froude number.

The quantitative measure of the variation of level of clustering at different Froude numbers is shown in Figure 7. We can observe that the radial distribution function $g(R)$ at contact significantly decreases with increasing Froude number by several times. For example, $g(R) = 10.7$ at $Fr_p = 0.0$ and it reduces to $g(R) = 2.6$ at $Fr_p = 4.71$, particles distribute more uniformly under large drift velocity.

When particles fall in turbulent flows, the interaction time scale between particles and turbulence reduces and particles tends to get less fluctuating velocity from the turbulent flows, thus the relative velocity between particles reduces. The radial

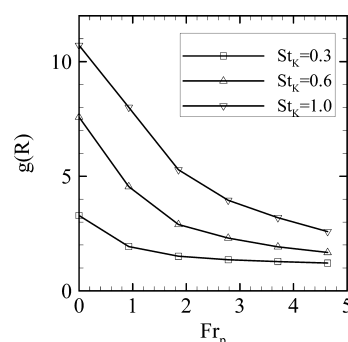


Figure 7. RDF $g(R)$ of particles at different Froude numbers.

relative velocity at contact is an important parameter for particle collision rate which is defined as

$$W_r(R) = \left\langle \left| (\mathbf{V}_{p,1} - \mathbf{V}_{p,2}) \cdot \frac{\mathbf{r}}{r} \right| \right\rangle_p \quad (20)$$

where $r = |\mathbf{r}| = |\mathbf{Y}_{p,1} - \mathbf{Y}_{p,2}|$ is the separation between two particles, $r = R = d_p$, $\mathbf{V}_{p,1}$, $\mathbf{V}_{p,2}$ are the velocities of the two particles, $\langle \bullet \rangle_p$ denotes the average over particle pairs with the separation of collision radius $R = d_p$. Figure 8 shows $W_r(R)$

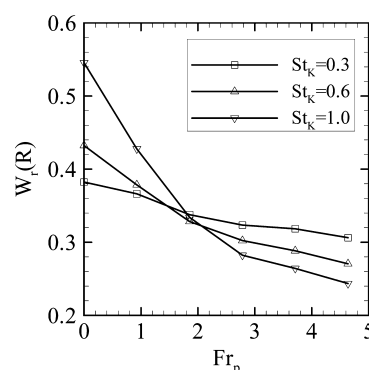


Figure 8. Variation of radial relative velocity $W_r(R)$ with Froude numbers.

decreases with Froude numbers. When $Fr_p < 2$, $W_r(R)$ increases with particle Stokes number; when $Fr_p > 2$, the relative velocity is smaller for particles at larger Stokes numbers.

The collision rate is important for turbulent coagulation of liquid droplets and solid reaction between particles.^{16,17} The direct consequences of the reduction of $g(R)$ and $W_r(R)$ by increasing Froude numbers is that the reduction of the collision rate between particles. The collision rate of the monodispersed particles is expressed as

$$N_c = 2\pi R^2 g(R) W_r(R) \frac{n_0^2}{2} \quad (21)$$

where $n_0 = N_p/(2\pi)^3$ is the average particle number density and N_p is the total particle number in the flow domain. Figure 9 shows that the collision rate decreases with Froude numbers.

3.4. RDF and Relative Velocity of Finite-Size Particles.

In this subsection, we shall study the radial distribution function and radial relative velocity of finite-size particles in the particle-resolved simulation in decaying isotropic turbulence. Table 2 lists the parameters in simulations using the lattice Boltzmann method, where N is the grid number, d_p is the nondimensional

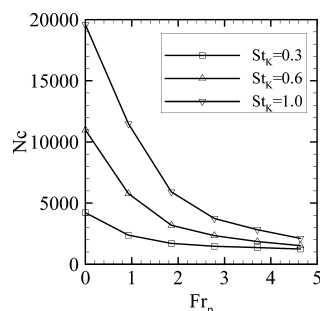


Figure 9. Particle collision rate with different Froude numbers.

particle diameter in lattice unit, N_p is the total particle number, Φ_V is volume fraction, and Φ_m is mass fraction.

The initial velocity field at $t = 0$ was specified by a Gaussian field with a prescribed kinetic energy spectrum as

$$E(k) = \left(\frac{3u'^2}{2} \right) \left(\frac{k}{k_p} \right)^2 \exp \left(-\frac{k}{k_p} \right) \quad (22)$$

where k is the wavenumber, k_p is the wavenumber containing peak energy, and u' is the initial rms velocity. Before releasing particles in the turbulent flow, a relaxation process is carried out via the nonlinear cascade over different scales. The nonlinear cascade is established when velocity-derivative skewness is about -0.50 as shown in Figure 10. After that, the particles are released in the domain at random locations with a gap distance of at least two grids. The initial translational velocities of particles are set as the instantaneous fluid velocity at the particle center, and angular velocity is set to be zero. The gravity was set to zero. The simulations are run from $t = 0$ to $t = 4.28T_{e,0}$, where the initial eddy turnover time $T_{e,0} = u'^2/\varepsilon$. The flow fields are well resolved as shown by $k_{\max}\eta > 1$ for the whole time interval.

In the particle-resolved simulation, when particles are released into the flow, the coupling between particles and fluid is automatically established through the moving surfaces of finite-size particles. Figure 11 shows snapshots of vorticity contour and particle location on the plane $z = 128.5$ in the simulation of case 4 at $t = 1.69T_{e,0}$. The different areas of circles are due to the different relative positions of spheres to the plane $z = 128.5$.

We can observe that the presence of finite-size particles is often associated with high vorticity values, suggesting that motion of finite-size particles can generate small-scale flow structures near particles. The disturbance near particles is visible. The clustering of finite-size particles is weak compared with the point particles at similar Stokes numbers. This is due to the fact that the size of particles is at the same scale around the Taylor microscale, and the centrifugal effects of the small scale vortical motions on particle motions are weak. Figure 12

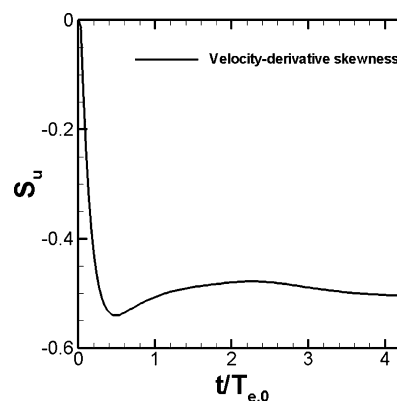


Figure 10. Velocity-derivative skewness of the turbulent flow versus time.

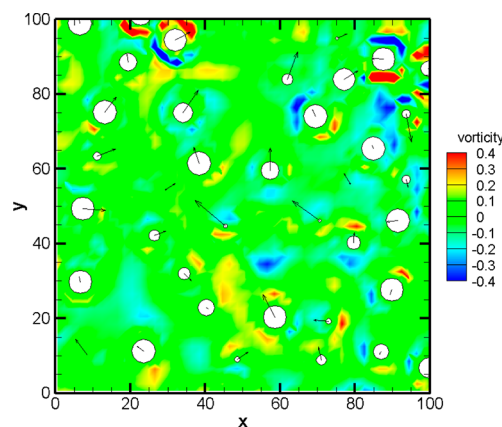


Figure 11. Snapshot of vorticity contour and particle location on a plane $z = 128.5$ in the 256^3 simulation of case 4 at $t = 1.69T_{e,0}$.

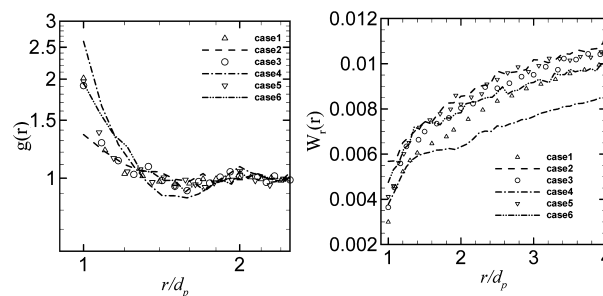


Figure 12. Radial distribution function and radial relative velocity of finite-size particles.

shows the variation of the radial distribution function and relative velocity of particles with the separation distance r . From Figure 12a, we can observe that the clustering is only obvious at very near contact, which is caused by the influence of the short-

Table 2. Parameters for Particle-Resolved Simulations

case no.	N^3	d_p	ρ_p/ρ_f	N_p	d_p/η	d_p/λ	Φ_V	Φ_m	τ_p/τ_K
1	256^3	8.0	1.2	6258	7.62	0.87	0.1	0.12	3.87
2	256^3	8.0	3.13	3130	7.62	0.87	0.05	0.14	10.08
3	256^3	10.0	1.2	3204	9.52	1.08	0.1	0.12	6.04
4	256^3	10.0	2.0	6408	9.52	1.08	0.2	0.33	10.08
5	256^3	12.0	1.2	1854	11.43	1.30	0.1	0.12	8.71
6	256^3	12.0	2.0	2782	11.4	1.30	0.1	0.26	14.51

range hydrodynamic interactions. This is consistent with the previous experimental results by Xu and Bodenschatz⁴⁰ that inertial particles with sizes larger than the Kolmogorov scale in turbulent flows have little clustering. In a study by Ladd⁴¹ on fully resolved settling spheres, a strong increase in the radial distribution function at short separations is also observed. For the same volume fraction, the values of $g(r)$ are almost unchanged. However, for the same Stokes number, the larger volume fraction leads to larger $g(r)$. When the separation is larger than $1.5D$, particles almost uniformly distribute in the flow fields.

From Figure 12b, we found that radial relative velocity is identical for the same volume fraction. And the value of radial relative velocity decreases with increasing volume fraction. Since the larger volume fraction can lead to a smaller turbulent kinetic energy, which will reduce the fluctuating velocities of particles and thus reduce the relative velocity between particles.

4. CONCLUSIONS

Particle clustering is ubiquitous in the riser of fast fluidized beds, which reduces the heat and mass transfer rates in the flows. How to control the level of clustering is very crucial to improve the reaction efficiency in the reactors. In this paper, we have studied the effects of mean drift velocity on particle clustering, which could be caused by gravity or external electric force for charged particles at particle Stokes number less than unit. The conclusions that can be drawn from the present study are as follows: (1) The drift velocity can reduce the level of clustering and the relative velocity in the turbulent flows for $St_K \leq 1$. As a consequence, the turbulent collision rate between particles is reduced. (2) The particles of size larger than the characteristic scales of turbulent flows are weakly clustering only at small separations. The results obtained propose a potential approach to control the level of particle clustering by producing a mean velocity between particles and fluids in turbulent flows in chemical engineering reactors.

AUTHOR INFORMATION

Corresponding Author

*Tel.: 86-10-82543969. Fax: 86-10-82543408. E-mail: hgw@lnm.imech.ac.cn.

Notes

The authors declare no competing financial interest.

ACKNOWLEDGMENTS

This work is supported by NSFC under Nos. 11072247, 11021262, 11232011 and NSAF under No.U1230126. J.G.D. would like to thank Professor Lian-Ping Wang at University of Delaware, USA, for the discussions during the work and Professor Jinghai Li at the Institute of Process Engineering, Chinese Academy of Sciences, for help and support in the work.

DEDICATION

In memory of Professor Mooson Kwauk at the Institute of Process Engineering, Chinese Academy of Sciences, who has recently passed away.

ABBREVIATIONS

CFL = Courant–Friedrichs–Lewy
DLM = distributed Lagrange-multiplier method
DNS = directive numerical simulation

EMMS = energy minimization multiscale
IBM = immersed boundary method
LBM = lattice-Boltzmann method
PPDNS = point particle DNS
PRDNS = particle-resolved DNS
RDF = radial distribution function
MRT-LBE = multiple-relaxation-time lattice-Boltzmann equation

REFERENCES

- (1) Li, J. H.; Kwauk, M. *Particle-Fluid Two-Phase Flow - the Energy-Minimization Multi-Scale Method*; Metallurgical Industry Press: Beijing, 1994.
- (2) Jin, G. D.; He, G.-W.; Wang, L.-P. Large-Eddy Simulation of Turbulent Collision of Heavy Particles in Isotropic Turbulence. *Phys. Fluids* **2010**, *22*, 055106.
- (3) Wang, L.-P.; Stock, A. D. Dispersion of Heavy Particles by Turbulent Motion. *J. Atmos. Sci.* **1993**, *50* (13), 1897–1913.
- (4) Ayala, O.; Rosa, B.; Wang, L.-P. Effects of Turbulence on the Geometric Collision Rate of Sedimenting Droplets. Part 2. Theory and Parameterization. *New J. Phys.* **2008**, *40*, 075016.
- (5) Agrawal, K.; Loezos, P. N.; Syamlal, M.; Sundaresan, S. The Role of Meso-Scale Structures in Rapid Gas-Solid Flows. *J. Fluid Mech.* **2001**, *445*, 151–185.
- (6) Zhang, D.; VanderHeyden, W. B. The Effects of Mesoscale Structures on the Macroscopic Momentum Equations for Two-Phase Flows. *Int. J. Multiphase Flow* **2002**, *28*, 805–822.
- (7) Chalermsoonsuwan, B.; Piumsomboon, P.; Gidaspow, D. Kinetic Theory Based Computation of PSRI Riser: Part I-Estimate of Mass Transfer Coefficient. *Chem. Eng. Sci.* **2009**, *64*, 1195–1211.
- (8) Reade, W. C.; Collins, L. R. Effects of Preferential Concentration on Turbulent Collision Rates. *Phys. Fluids* **2000**, *12*, 2530–2540.
- (9) Yang, N.; Wang, W.; Ge, W.; Li, J. H. CFD Simulation of Concurrent up Gas–Solid Flow in Circulating Fluidized Beds with Structure-Dependent Drag Coefficient. *Chem. Eng. J.* **2003**, *96*, 71–80.
- (10) Yang, N. A Multi-Scale Framework for CFD Modelling of Multi-Phase Complex Systems Based on the EMMS Approach. *Prog. Comp. Fluid Dyn.* **2012**, *12*, 220–229.
- (11) Wang, W.; Li, J. Simulation of Gas-Solid Two-Phase Flow by a Multi-Scale CFD Approach—of the EMMS Model to the Sub-Grid Level. *Chem. Eng. Sci.* **2007**, *62*, 208–231.
- (12) Wang, J.; Ge, W.; Li, J. Eulerian Simulation of Heterogeneous Gas-Solid Flows in CFB Risers: EMMS-Based Sub-Grid Scale Model with a Revised Cluster Description. *Chem. Eng. Sci.* **2008**, *63*, 1553–1571.
- (13) Wang, L.-P.; Maxey, M. R. Settling Velocity and Concentration Distribution of Heavy Particles in Homogeneous Isotropic Turbulence. *J. Fluid Mech.* **1993**, *256*, 27–68.
- (14) Tang, L.; Wen, F.; Yang, Y.; Crowe, C. T.; Chung, J. N.; Troutt, T. R. Self-Organizing Particle Dispersion Mechanism in a Plane Wake. *Phys. Fluids* **1992**, *4*, 2244–2251.
- (15) Bec, J.; Biferale, L.; Cencini, M.; Lanotte, A.; Musacchio, S.; Toschi, F. Heavy Particle Concentration in Turbulence at Dissipative and Inertial Scales. *Phys. Rev. Lett.* **2007**, *98*, 084502.
- (16) Sundaram, S.; Collins, L. R. Collision Statistics in an Isotropic, Particle-Laden Turbulent Suspension. *J. Fluid Mech.* **1997**, *335*, 75–109.
- (17) Wang, L.-P.; Wexler, A. S.; Zhou, Y. Statistical Mechanical Description and Modelling of Turbulent Collision of Inertial Particles. *J. Fluid Mech.* **2000**, *415*, 117–153.
- (18) Martínez, J.; Chehata, D.; van Gils, D. P. M.; Sun, C.; Lohse, D. On Bubble Clustering and Energy Spectra in Pseudo-Turbulence. *J. Fluid Mech.* **2010**, *650*, 287–306.
- (19) Monchaux, R.; Bourgoïn, M.; Cartellier, A. Preferential Concentration of Heavy Particles: A Voronoi Analysis. *Phys. Fluids* **2010**, *22*, 103304.
- (20) Oblgado, M.; Missaoui, M.; Monchaux, R.; Cartellier, A.; Bourgoïn, M. Reynolds Number Influence on Preferential Concen-

tration of Heavy Particles in Turbulent Flows. *J. Phys.: Conf. Ser.* **2011**, 318, 052015.

(21) Tagawa, Y.; Mercado, J. M.; Prakash, V. N.; Calzavarini, E.; Sun, C.; Lohse, D. Three-Dimensional Lagrangian Voronoï Analysis for Clustering of Particles and Bubbles in Turbulence. *J. Fluid Mech.* **2012**, 693, 201–205.

(22) Fiabane, L.; Zimmermann, R.; Volk, R.; Pinton, J.-F.; Bourgoin, M. Clustering of Finite-Size Particles in Turbulence. *Phys. Rev. E* **2012**, 86, 035301(R).

(23) Calzavarini, E.; Kerscher, M.; Lohse, D.; Toschi, F. Dimensionality and Morphology of Particle and Bubble Clusters in Turbulent Flow. *J. Fluid Mech.* **2008**, 607, 13–24.

(24) Chen, S. Y.; Doolen, G. D. Lattice Boltzmann Method for Fluid Flows. *Annu. Rev. Fluid Mech.* **1998**, 30, 329–364.

(25) Aidun, C. K.; Clausen, J. R. Lattice-Boltzmann Method for Complex Flows. *Annu. Rev. Fluid Mech.* **2010**, 42, 439–472.

(26) Wang, L. M.; Zhou, G. F.; Wang, X. W.; Xiong, Q. G.; Ge, W. Direct Numerical Simulation of Particle-Fluid Systems by Combining Time-Driven Hard-Sphere Model and Lattice Boltzmann Method. *Particuology* **2010**, 8, 379–382.

(27) Eswaran, E.; Pope, S. B. An Examination of Forcing in Direct Numerical Simulations of Turbulence. *Comput. Fluids* **1988**, 16, 257–278.

(28) Wang, L. P.; Wexler, A. S.; Zhou, Y. On the Collision Rate of Small Particles in Isotropic Turbulence Part I. Zero-Inertia Case. *Phys. Fluids* **1998**, 10, 266–276.

(29) Maxey, M. R.; Riley, J. J. Equation of Motion for a Small Rigid Sphere in a Nonuniform Flow. *Phys. Fluids* **1983**, 26, 883–889.

(30) Qureshi, N. M.; Bourgoin, M.; Baudet, C.; Cartellier, A.; Gagne, Y. Turbulent Transport of Material Particles: an Experimental Study of Finite-Size Effects. *Phys. Rev. Lett.* **2007**, 99, 184502.

(31) Naso, A.; Prosperetti, A. The Interaction between a Solid Particle and a Turbulent Flow. *New J. Phys.* **2010**, 12, 033040.

(32) Zaichik, L.; Alipchenkov, V. M. A Model for Predicting the Acceleration Variance of Arbitrary-Density Finite-Size Particles in Isotropic Turbulence. *Int. J. Multiphase Flow* **2011**, 37, 236–240.

(33) Uhlmann, M. Interface-Resolved Direct Numerical Simulation of Vertical Particulate Channel Flow in the Turbulent Regime. *Phys. Fluids* **2008**, 20, 053305.

(34) Shao, X. M.; Wu, T. H.; Yu, Z. S. Fully Resolved Numerical Simulation of Particle-Laden Turbulent Flow in a Horizontal Channel at a Low Reynolds Number. *J. Fluid. Mech.* **2012**, 693, 319–344.

(35) Gao, H.; Li, H.; Wang, L.-P. Lattice Boltzmann Simulation of Turbulent Flow Laden with Finite-Size Particles. *Comp. Math. Appl.* **2011**, DOI: 10.1016/j.camwa.2011.06.028.

(36) d'Humieres, D.; Ginzburg, I.; Krafczyk, M.; Lallemand, P.; Luo, L. S. Multiple-Relaxation Time Lattice Boltzmann Models in Three-Dimensions. *Phil. Trans. R. Soc. Lond.* **2002**, A360, 437–451.

(37) Qian, Y. H.; d'Humieres, D.; Lallemand, P. Lattice BGK Models for Navier-Stokes Equation. *Europhys. Lett.* **1992**, 17 (6), 479–484.

(38) Feng, Z. G.; Michaelides, E. E. Proteus: a Direct Forcing Method in the Simulations of Particulate Flows. *J. Comput. Phys.* **2005**, 202, 20–51.

(39) Monchaux, R.; Bourgoin, M.; Cartellier, A. Analyzing Preferential Concentration and Clustering of Inertial Particles in Turbulence. *Int. J. Multiphase Flow* **2012**, 40, 1–18.

(40) Xu, H. T.; Bodenschatz, E. Motion of Inertial Particles with Size Larger Than Kolmogorov Scale in Turbulent Flows. *Phys. D* **2008**, 237, 2095–2100.

(41) Ladd, A. J. C. Sedimentation of Homogeneous Suspensions of Non-Brownian Spheres. *Phys. Fluids* **1997**, 9, 491–499.